Pure and Linear Frequency-Conversion Temporal Metasurface

Sajjad Taravati* and George V. Eleftheriades
The Edward S. Rogers Sr. Department of Electrical and Computer Engineering, University of Toronto, Toronto, Ontario M5S 3H7, Canada

(Received 10 February 2021; revised 3 May 2021; accepted 19 May 2021; published 4 June 2021)

Metasurfaces are ultrathin structures which are constituted by an array of subwavelength scatterers with designable scattering responses. They have opened up unprecedented exciting opportunities for extraordinary wave engineering processes. On the other hand, frequency converters have drawn wide attention due to their vital applications in telecommunication systems, healthcare devices, radio astronomy, military radars, and biological sensing systems. Here, we show that a spurious-free and linear frequency-converter metasurface can be realized by leveraging unique properties of engineered transmissive temporal supercells. Such a metasurface is formed by time-modulated supercells, which are composed of temporal and static patch resonators and phase shifters. This represents a frequency-converter metasurface possessing large frequency-conversion ratio with controllable frequency bands and transmission magnitude. In contrast to conventional nonlinear mixers, the proposed temporal frequency converter offers a linear response. In addition, by taking advantage of the proposed surface-interconnector-phaser-surface (SIPS) architecture, a spurious-free and linear frequency conversion is achievable, where all undesired mixing products are strongly suppressed. The proposed metasurface may be digitally controlled and programmed through a field programmable gate array. This makes the spurious-free and linear frequency-converter metasurface a prominent solution for wireless and satellite telecommunication systems, as well as invisibility cloaks and radars. This study opens a way to realize more complicated and enhanced-efficiency spectrum-changing metasurfaces.

DOI: 10.1103/PhysRevApplied.15.064011

I. INTRODUCTION

Frequency conversion is a vital task in telecommunication systems, where the frequency of the input signal is translated into a greater or smaller value, i.e., up-converted in transmitters and down-converted in receivers. Practical frequency conversion is desirable to produce large frequency-conversion ratios, where the frequency of the input signal is translated from a frequency band to another frequency band, e.g., from UHF band to L band. Conventional nonlinear mixers produce unsought spurious signals as a result of the harmonic mixing of the radio-frequency (RF) and local oscillator (LO) signals. For single-tone RF and LO signals, the spurious signal frequencies correspond to the $i\omega_{\mathrm{RF}} + j\,\omega_{\mathrm{LO}}$ harmonic products, with i and j being any integers. However, multi-tone RF and LO signals yield a much more unsought spurious frequencies including the principal $i\omega_{\mathrm{RF}} + j\,\omega_{\mathrm{LO}}$ harmonic products for each RF tone combined with each LO tone individually plus the cross-modulation products between multiple RF and LO tones.

A quasi-pure frequency conversion is conventionally achieved by integration of frequency mixers with bandpass filters which typically result in high insertion loss and large profile structure. Frequency mixers are usually formed by nonlinear components, e.g., Schottky diodes, GaAs field-effect transistors (FETs) and complementary metal-oxide-semiconductor (CMOS) transistors [1–3], where the nonlinear response of the component results in generation of an infinite number of mixing products leading to a significant waste of power due to the transition of power to unwanted frequencies. Over the past few decades, several approaches have been proposed to realize harmonic-rejection mixers. Nevertheless, conventional nonlinear mixers, switching mixers, sub-sampling mixers and microwave photonic mixers, even in their most ideal operation regimes, still suffer from unwanted mixing products [1,4–6].

Space-time refractive-index modulation represents a prominent alternative approach for the realization of linear frequency mixers. Recently, space-time-modulated media have attracted a surge of interest thanks to their extraordinary capability in multifunctional operations, e.g., mixer-duplexer-antennas [7], unidirectional beam splitters [8], nonreciprocal filters [9], and signal coding metagratings [10]. In addition, a large number of versatile and high-efficiency electromagnetic systems have been reported recently based on the unique properties of space-time

*sajjad.taravati@utoronto.ca

 © 2021 American Physical Society

modulation, including space-time metasurfaces for advanced wave engineering and extraordinary control over electromagnetic waves [11–32], nonreciprocal platforms [33–41], frequency converters [19,42], and time-modulated antennas [43,44]. Such strong capabilities of space-time-modulated media is due to their unique interactions with the incident field [22,34,45–56].

Periodic time modulation is a promising approach for *linear* frequency mixing thanks to the lack of harmonics of the incident frequency. This is due to the fact that the temporal medium is only periodic with respect to the modulation frequency ω_m. Time modulation provides the required energy for transition from the fundamental temporal frequency ω_0 to an infinite number of time frequency harmonics $\omega_O = \omega_0 \pm n\omega_m$ and, hence, the output wave includes time harmonics of the modulation wave [34,42,57]. Although the lack of harmonics of the incident signal in the output signal represents an advantage of time-modulated mixers over conventional nonlinear mixers, the existence of harmonics of the modulation in the output signal is still problematic and indicates a nonpure frequency conversion and waste of energy [19]. Another drawback of previously reported time-modulated mixers is their extra-small frequency-conversion ratio [19], which is impractical especially for telecommunication systems, where large frequency conversions are required.

Herein, we introduce a technique for the realization of spurious-free and linear frequency-converter metasurfaces based on a time-modulation technique, where harmonic electromagnetic transitions in temporally periodic systems are prohibited by *tailored* photonic band gaps introduced by the engineered spatial aperiodicity of the supercells. The proposed surface-interconnector-phaser-surface (SIPS) architecture acts inherently as a multiband bandpass filter, that is, providing multichannel bandpass transmissions and strong stopbands which are leveraged for local suppression of undesired time harmonics. Such local suppressions lead to a spurious-free and linear frequency conversion and inhibits the leakage of incident wave to undesired time harmonics which would have yielded a substantial waste of power. The proposed frequency-converter metasurface inherits the linearity property of time modulation. In addition, the frequency bands of the frequency-converter metasurface may be controlled via time-modulation parameters as well as patch resonators.

II. THEORY AND CONCEPT

A. Metasurface operation

Figure 1 presents the conceptual illustration of programmable spurious-free and linear frequency conversion induced by a temporal metasurface. The metasurface is characterized with the general time-modulated permittivity of $\epsilon(t) = f(\omega_m t)$, where $f(.)$ represents a periodic function. The metasurface is illuminated by a plane wave from the left side. We show that with proper design of the metasurface supercells, a spurious-free and linear frequency up-conversion, from $\omega_0 - \omega_m$ to ω_0, and a spurious-free and linear frequency down-conversion, from $\omega_0 + \omega_m$ to ω_0, can be achieved. The functionality and frequencies of the metasurface can be controlled via a field-programmable gate array (FPGA).

Figure 2(a) shows wave propagation and radiation in a standard half-wavelength microstrip patch resonator antenna where the injected signal in the feed line of the patch antenna is efficiently radiated to air. Here, the patch

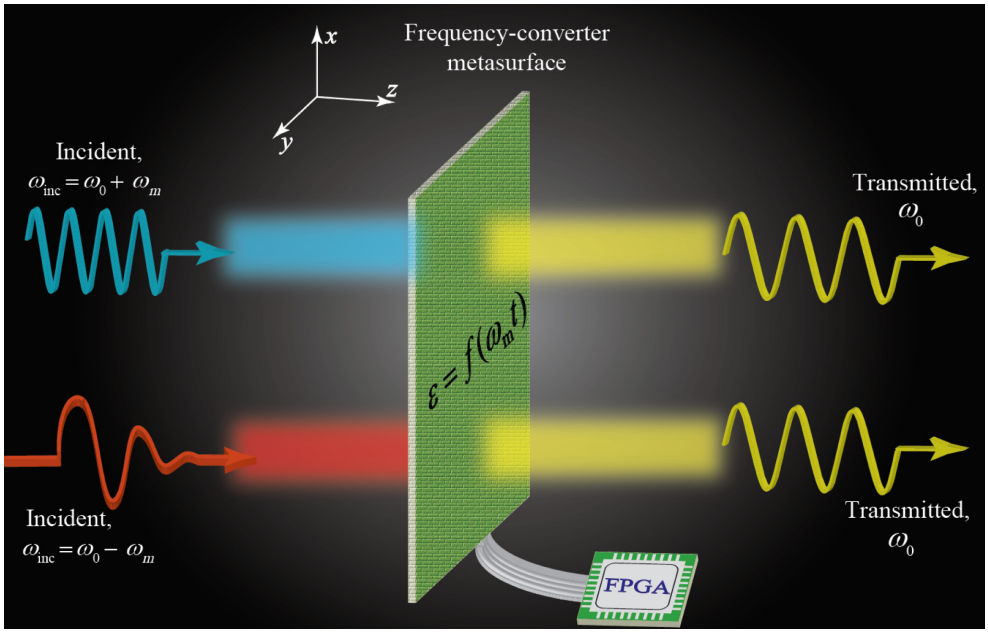

FIG. 1. Conceptual illustration of programmable spurious-free and linear frequency conversion induced by a temporal metasurface.

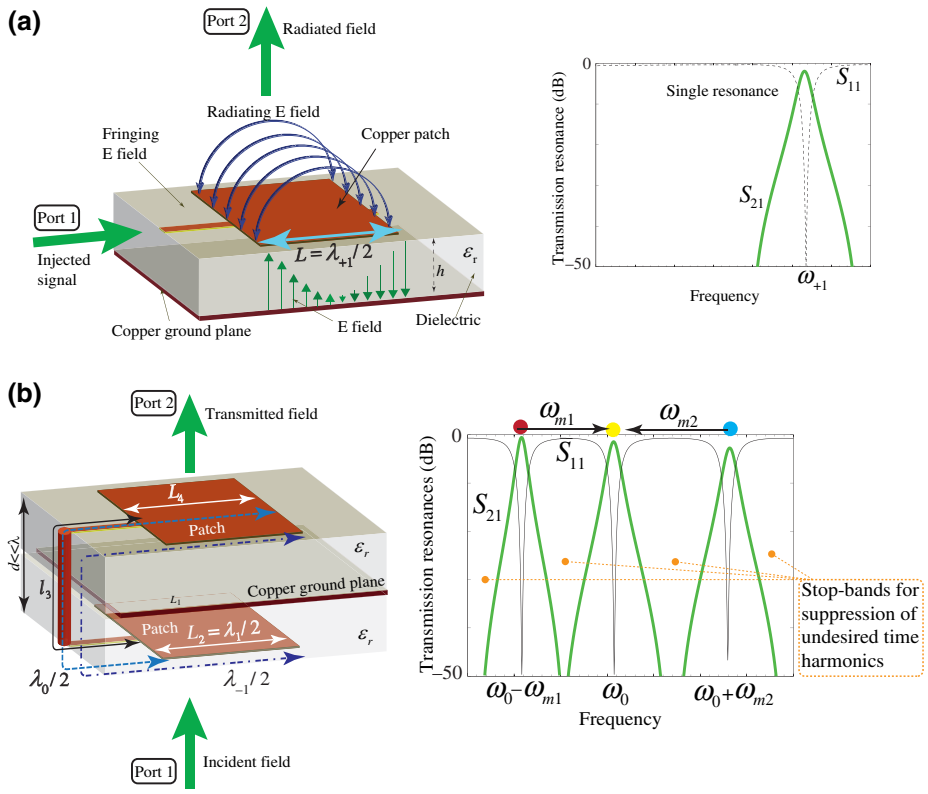

FIG. 2. Transmission resonances in (a) a standard patch antenna introducing a single transmission resonance and (b) a SIPS architecture composed of two interconnected microstrip patch resonators, introducing multiple in-band full-transmission resonances as well as strong out-of-band reflection.

resonator antenna introduces a single resonance providing full-transmission from the feeding line to air at ω_1 corresponding to the resonant frequency of the patch antenna. At this resonance, the length of the patch antenna corresponds to the half-wavelength of the incident frequency, that is, $L = \lambda_1/2$.

Figure 2(b) depicts a nonmodulated single-fed SIPS supercell where two single-fed patch resonators are interconnected in a three-layer architecture, composed of two conductor layers mounted on two dielectric layers and shielded from each other by a copper ground plane layer. In contrast to the single patch resonator in Fig. 2(a), here the structure introduces at least three major resonances, corresponding to the single patch resonance and coupled structure resonances, as shown in Fig. 2(b). As a result, the incident field from the bottom (top) of the structure is transmitted to the top (bottom) of the SIPS architecture at three different frequencies, that is, $\omega_{-1} = \omega_0 - \omega_{m1}$, ω_0, and $\omega_{+1} = \omega_0 + \omega_{m2}$. Here, ω_{m1} represents the local frequency for down-conversion and ω_{m2} represents the local frequency for up-conversion. As a result, with proper design of the SIPS structure, controllable full-transmission passbands can be achieved at the desired frequencies, and stopbands exhibiting large suppressions can be achieved at undesired frequencies, for example, ω_{-2}, ω_{-3}, ω_{+2}, and ω_{+3}. This property of the proposed SIPS architecture offers an outstanding opportunity for spurious-free and linear frequency conversion when integrated with time modulation.

B. Scattering parameters for metasurface passbands

Figure 3(a) shows an unfolded version of the single-fed SIPS structure in Fig. 2(b), where a pair of single-fed patch resonators with lengths L_2 and L_4 are interconnected via interconnections of length l_3. The wavenumbers k of such inhomogeneous microstrip transmission lines depend on their width [58]. Hence, the wavenumbers are different in each region, that is, $k_1(=k_5) \neq k_2(=k_4) \neq k_3$. The electric field in the sth region ($s = 1, \ldots, 5$) is composed of forward and backward waves as $E_s = V_s^+ e^{-jk_s z} + V_s^- e^{jk_s z}$, where V_s^+ and V_s^- are the amplitudes of the forward and backward waves, respectively, and k_s is the wavenumber. It should be noted that the backward waves, propagating along the $-z$ direction, are due to reflection at the different interfaces between adjacent regions. Upon application of boundary conditions at the interface between regions s and $s+1$, the total transmission and total reflection coefficients between regions s and $s+1$ are found as as [59]

$$\widetilde{T}_{s+1,s} = \frac{V_{s+1}^+}{V_s^+} = \frac{T_{s+1,s} e^{-j(k_s - k_{s+1})z}}{1 - R_{s+1,s}\widetilde{R}_{s+1,s+2} e^{-j2k_{s+1}l_{s+1}}}, \tag{1a}$$

$$\widetilde{R}_{s,s+1} = \frac{R_{s,s+1} + \widetilde{R}_{s+1,s+2} e^{-j2k_{s+1}l_{s+1}}}{1 + R_{s,s+1}\widetilde{R}_{s+1,s+2} e^{-j2k_{s+1}l_{s+1}}}. \tag{1b}$$

where $R_{s,s+1} = (\eta_{s+1} - \eta_s)/(\eta_{s+1} + \eta_s)$, with η_s being the intrinsic impedance of region s, is the local reflection coefficient within region s between regions s and $s+1$,

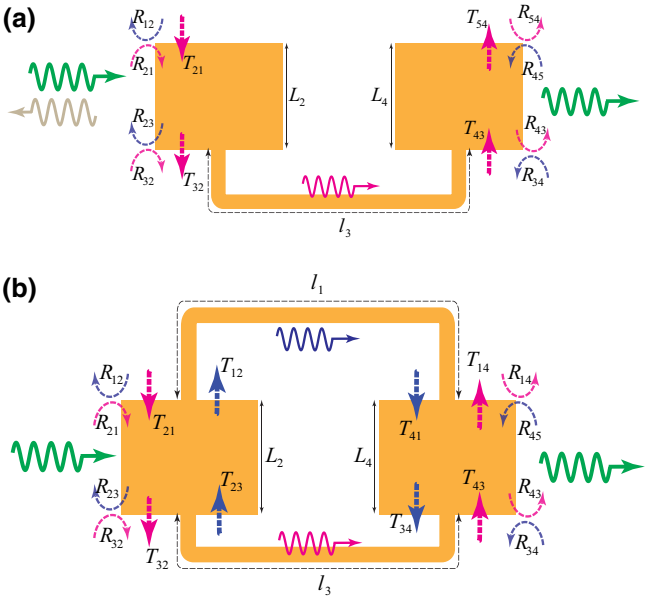

FIG. 3. Total transmission following multiple transmissions and reflections inside (a) a single-interconnected single-fed patch antenna pair and (b) a double-interconnected double-fed patch antenna pair.

and $R_{s+1,s} = -R_{s,s+1}$. The local transmission coefficient from region s to region $s+1$ reads $T_{s+1,s} = 1 + R_{s,s+1}$. It should be noted that the term $e^{-j(k_s - k_{s+1})z}$ in (1a) indicates that, due to the nonuniformity of the structure in Fig. 2(a), a phase shift occurs at each interface which corresponds to the difference between the wavenumbers in adjacent regions. We assume $k_1 = k_5 = k_0$, $k_2 = k_4 = k_p$, and $k_3 = k_t$ the wavenumbers in the air, in the two patches, and in the interconnecting transmission line, respectively. We consider $L_2 = L_4 = L$, $R_{1,2} = -R_{2,1} = -R_{4,5} = R_p$, and $R_{2,3} = -R_{3,2} = -R_{3,4} = R_{4,3} = R_t = (\eta_t - \eta_p)/(\eta_t + \eta_p)$ the local reflection coefficient at the interface between a patch and the interconnecting transmission line.

Then, the total transmission coefficient for the single-fed SIPS metasurface of Fig. 3(a), from region 1 to region 5, reads

$$S_{21} = T_{5,1} = \prod_{s=1}^{4} \widetilde{T}_{s+1,s} e^{-jk_s l_s}, \tag{2}$$

where $\widetilde{T}_{s+1,s}$, for $s = 1, \ldots, 4$ is provided by (1a) with (1b). The total transmission coefficient from the nonmodulated single-fed SIPS supercell in Fig. 3(a) is found in terms of local reflection coefficients as

$$S_{21} = \frac{(1 - R_{12}^2)(1 - R_{23}^2) e^{j(k_p + k_0 - 2k_3) l_3}}{(R_{12}R_{23} + e^{j2k_p L})^2 - (R_{23} e^{j2k_p L} + R_{12})^2 e^{-j2k_3 l_3}}. \tag{3}$$

The term $e^{-j2k_t l_3}$ in the denominator of this expression corresponds to the round-trip propagation through the middle transmission line, the multiplication of which by $e^{j4k_p L}$ in the adjacent bracket corresponds to the patch-line-patch coupled-structure resonance, with length $2L + l_3$.

Figure 3(b) shows the unfolded version of the double-fed SIPS structure, where a pair of double-fed patch resonators with lengths L_2 and L_4 are double-interconnected via two interconnections possessing different lengths, that is, l_1 and l_2. We assume that the upper interconnection with length l_2 represents the region 1. The total transmission coefficient from the double-fed SIPS structure in Fig. 3(b) reads

$$S_{21} = \frac{(1 - R_{12}^2)(1 - R_{23}^2) e^{j(k_p + k_0 - 2k_3) l_3}}{(R_{12}R_{23} + e^{j2k_p L})^2 - (R_{23} e^{j2k_p L} + R_{12})^2 e^{-j2k_3 l_3}} - \frac{(1 - R_{32}^2)(1 - R_{21}^2) e^{j(k_p + k_0 - 2k_1) l_1}}{(R_{32}R_{21} + e^{j2k_p L})^2 - (R_{21} e^{j2k_p L} + R_{32})^2 e^{-j2k_1 l_1}}. \tag{4}$$

Equation (4) highlights the effect of l_1 and l_3 on the transmission through the double-fed SIPS in Fig. 3(b). Hence, by changing the phase shift through l_1 and l_3 the frequency and magnitude of the transmission parameter S_{21} is controlled. In general, fixed transmission-line-based phase shifters with lengths l_1 and l_3 can be replaced by two digitally controlled phase shifters.

C. Time modulation characterization

Figure 4 sketches the wave propagation and transmission through the time-modulated supercell, characterized with two time-varying resonators possessing a periodic time-dependent permittivity, i.e.,

$$\epsilon(t) = \epsilon_{\text{ant}} + \epsilon_{\text{mod}} \cos(\omega_m t), \tag{5}$$

where ϵ_{ant} is the average effective permittivity of the patch antennas, ϵ_{mod} denotes the modulation amplitude and ω_m denotes the modulation frequency. The electric field inside each of these two time-varying resonators may be expressed based on the superposition of two supported

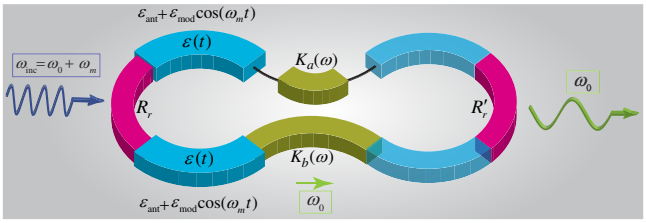

FIG. 4. Schematic representation and operation principle of the time-modulated SIPS radiating supercell.

space-time harmonic fields, i.e.,

$$E_m(\zeta,t) = a(\zeta)e^{-i(k_a\zeta-\omega_0 t)} + b(\zeta)e^{-i(k_b\zeta-(\omega_0+\omega_m)t)}. \quad (6)$$

The corresponding wave equation reads $c^2\partial^2\mathbf{E}/\partial\zeta^2 = \partial^2[\epsilon_{\rm eq}(t)\mathbf{E}]/\partial t^2$. Inserting the electric field in (6) into the wave equation results in

$$\left(\frac{\partial^2}{\partial\zeta^2}\right)\left[a(\zeta)e^{-i(k_a\zeta-\omega_0 t)} + b(\zeta)e^{-i(k_b\zeta-(\omega_0+\omega_m)t)}\right] = \frac{1}{c^2}\frac{\partial^2}{\partial t^2}\left(\left[\epsilon_{\rm ant} + \frac{\delta}{2}e^{i(\omega_m t)} + \frac{\delta}{2}e^{-i(\omega_m t)}\right]\left(a(\zeta)e^{-i(k_a\zeta-\omega_0 t)} + b(\zeta)e^{-i(k_b\zeta-(\omega_0+\omega_m)t)}\right)\right), \quad (7)$$

and applying the space and time derivatives, while using a slowly varying envelope approximation, multiply both sides with $\exp(i[k_a\zeta - \omega_0 t])$, which gives

$$\left[k_a^2 a(\zeta) - 2ik_a\frac{da(\zeta)}{d\zeta}\right] + \left[k_b^2 b(\zeta) - 2i(k_b)\frac{db(\zeta)}{d\zeta}\right]e^{i\omega_m t} = \frac{1}{c^2}\left(\left[\omega_0^2\epsilon_{\rm ant} + (\omega_0+\omega_m)^2\frac{\delta}{2}e^{i(\omega_m t)} + (\omega_0-\omega_m)^2\frac{\delta}{2}e^{-i(\omega_m t)}\right]a(\zeta) + \left[\omega_0^2\epsilon_{\rm ant} + (\omega_0+2\omega_m)^2\frac{\delta}{2}e^{i(\omega_m t)} + \omega_0^2\frac{\delta}{2}e^{-i(\omega_m t)}\right]b(\zeta)e^{i\omega_m t}\right), \quad (8)$$

Then, we apply $\int_0^{2\pi/\omega_m} dt$ to both sides of (8), which yields a coupled differential equation for the field coefficients, that is,

$$\frac{d}{d\zeta}\begin{bmatrix}a(\zeta)\\ b(\zeta)\end{bmatrix} = \begin{bmatrix}M_0 & C_0\\ C_1 & M_1\end{bmatrix}\begin{bmatrix}a(\zeta)\\ b(\zeta)\end{bmatrix}, \quad (9)$$

where $M_0 = i(k_{\rm ant}^2 - k_a^2)/(2k_a)$, $M_1 = i(k_0^2 - k_b^2)/(2k_b)$, $C_0 = i\delta k_0^2/(4k_a)$, and $C_1 = i\delta k_0^2/(4k_b)$. The solution to the coupled differential equation in (9) reads

$$a(\zeta) = \frac{E_0}{2\Delta}\left((M_0 - M_1 + \Delta)e^{\frac{M_0+M_1+\Delta}{2}\zeta}\right. \quad (10a)$$

$$\left. - (M_0 - M_1 - \Delta)e^{\frac{M_0+M_1-\Delta}{2}\zeta}\right), \quad (10b)$$

$$b(\zeta) = \frac{E_0 C_1}{\Delta}\left(e^{\frac{M_0+M_1+\Delta}{2}\zeta} - e^{\frac{M_0+M_1-\Delta}{2}\zeta}\right), \quad (10c)$$

where $\Delta = \sqrt{(M_0 - M_1)^2 + 4C_0C_1}$.

To determine the susceptibilities providing the response of the metasurface, we consider

$$\boldsymbol{D}(t) = \overline{\overline{\epsilon}}(t)\cdot\boldsymbol{E}(t) + \overline{\overline{\xi}}(t)\cdot\boldsymbol{H}(t), \quad (11a)$$

$$\boldsymbol{B}(t) = \overline{\overline{\zeta}}(t)\cdot\boldsymbol{E}(t) + \overline{\overline{\mu}}(t)\cdot\boldsymbol{H}(t). \quad (11b)$$

We then apply the generalized sheet transition condition (GSTC) method [60–62] for the analysis of zero-thickness metasurfaces. The metasurface is then characterized by the continuity equations of

$$\hat{z}\times\Delta\boldsymbol{H}(t) = j\omega\epsilon_0\overline{\overline{\chi}}_{ee}(t)\cdot\boldsymbol{E}_{\rm av}(t) + jk\overline{\overline{\chi}}_{em}(t)\cdot\boldsymbol{H}_{\rm av}(t), \quad (12a)$$

$$\Delta\boldsymbol{E}(t)\times\hat{z} = j\omega\mu_0\overline{\overline{\chi}}_{mm}(t)\cdot\boldsymbol{H}_{\rm av} + jk\overline{\overline{\chi}}_{me}(t)\cdot\boldsymbol{E}_{\rm av}(t), \quad (12b)$$

where Δ and the subscript "av" are the difference of the fields and the average of the fields between the two sides of the metasurface, respectively. Equation (12) gives the relation between the electromagnetic fields on the two sides of the metasurface and its susceptibilities, while assuming no normal susceptibility components. Finally, we may relate the susceptibilities in (12) to the constitutive parameters in (11), i.e.,

$$\overline{\overline{\epsilon}}(t) = \epsilon_0(\overline{\overline{I}} + \overline{\overline{\chi}}_{ee}(t)), \quad \overline{\overline{\mu}} = \mu_0(\overline{\overline{I}} + \overline{\overline{\chi}}_{mm}), \quad (13)$$

where $\overline{\overline{\xi}} = \overline{\overline{\chi}}_{em}/c_0 = 0$ and $\overline{\overline{\zeta}} = \overline{\overline{\chi}}_{me}/c_0 = 0$. One may characterize the metasurface based on temporal surface parameters (e.g., Ref. [63]) instead of the temporal permittivity and permeability (e.g., Ref. [11]). Nevertheless, the description of the involved physics and phenomena would be identical in both cases. To this end, we introduce effective permittivity and permeability parameters in Eq. (13) to establish a formal relation between these parameters.

III. EXPERIMENTAL RESULTS

To design the frequency-converter temporal metasurface, we first design the SIPS architecture in Figs. 5(a)

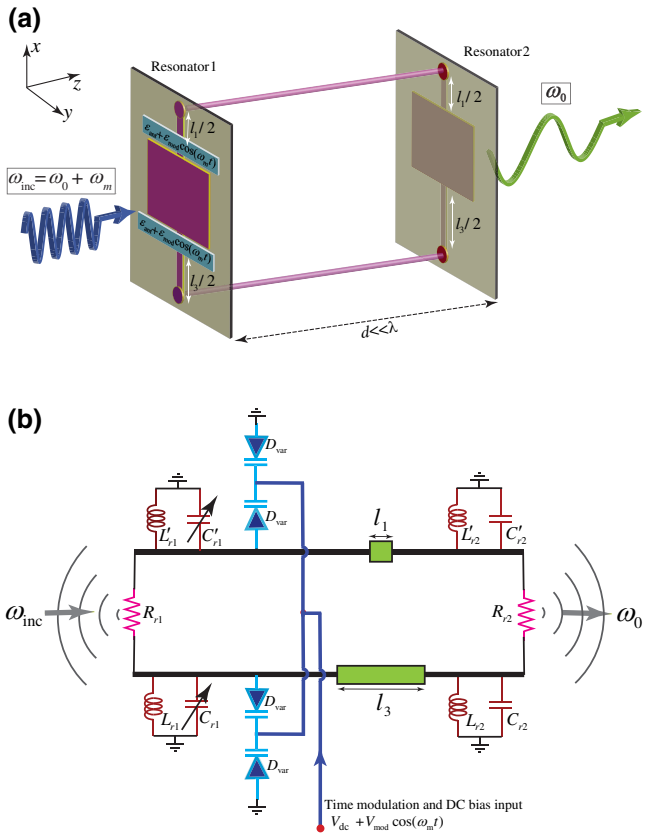

FIG. 5. Time-modulated SIPS supercell. (a) Realization using a temporal double-fed microstrip patch resonator and a non-modulated double-fed microstrip patch resonator. (b) Circuit model and realization of the temporal modulation using RF-biased varactors.

and 5(b) and determine the transmission of the SIPS using Eq. (4). To achieve the desired passbands and stopbands, we adjust the dimensions of the patch resonators and the length and width of the transmission-line-based phase shifters. The operation of the metasurface including passbands and the magnitude of the converted frequency harmonic can be fine-tuned in the lab through the DC bias of the varactors by determining the average capacitance of the varactors (corresponding to ϵ_{ant}), and the amplitude of the modulation signal wave (corresponding to ϵ_{mod}).

Figure 5(a) depicts the realization of the time-modulated SIPS supercell using a temporal double-fed microstrip patch resonator and a non-modulated double-fed microstrip patch resonator. Figure 5(b) shows a circuit model and realization of the temporal modulation using RF-biased varactors. Figure 6(a) illustrates the architecture of the fabricated proof-of-principle frequency-converter temporal metasurface. Figure 6(b) provides two photos showing the top and bottom views of the fabricated metasurfaces. The metasurface is realized using multilayer circuit technology, where two 10 in. × 10.5 in. RT5880 substrates with thickness $h = 31$ mil are assembled to realize a three metalization layer structure. The permittivity of the substrate is $\epsilon = \epsilon_r(1 - j\tan\delta)$, with $\epsilon_r = 2.2$ and $\tan\delta = 0.0009$ at 10 GHz. The middle conductor of the structure [shown in Fig. 6(a)] acts as the RF ground plane for the patch antennas and transmission lines. The DC bias and the modulation signal are both delivered to the supercells through the top conductor layer. One may deliver the DC bias and the modulation signal through the middle conductor sheet. Each side of the metasurface includes 16 microstrip patch resonators, where the dimensions of the 2 × 16 microstrip patches are 1.18 in. × 1.417 in. The connections between the conductor layers are provided by an array of circular metalized through holes, where 32 vias of 40 mil diameter provide grounding point at the top and bottom layers for varactors. In addition, 16 vias of 20 mil diameter are placed exactly at the center of patch resonator ensuring a DC null on the patches so that proper reverse-bias operation of varactors are guaranteed. Furthermore, the RF path connection between the two sides of the metasurface is provided by 32 via holes, with optimized dimensions of 157 mil for the via diameters, and 320 mil for the hole diameter in the via middle conductor ensuring that the RF through from the top layer to the bottom layer is safely isolated from the middle ground-plane conductor. For the varactors, we have utilized 64 BB837 silicon tuning varactor diodes manufactured by the Infineon Technologies.

Figures 7(a) and 7(b) show the experimental setup for measuring the scattering parameters of the static metasurface, i.e., $\omega_m = 0$.

Figures 8(a)–8(c) plot the experimental scattering parameters of the nonmodulated metasurface ($\omega_m = 0$) for different voltages corresponding to different ϵ_{ant}. Figure 8(a) shows that there are three major transmissions through the metasurface around 2.3, 3.3, and 5 GHz. Hence, we examine a frequency conversion from 2.3 to 3.3 GHz (corresponding to the modulation frequency $\omega_m =$ 1.06 GHz), and a frequency down-conversion from 5 to 3.3 GHz (corresponding to the modulation frequency $\omega_m =$ 1.79 GHz).

We shall stress that the transmission of the metasurface cannot be measured by a vector network analyzer, as the general scattering parameters measured by a vector analyzer are defined only for time-invariant systems. In general, all frequency converters, mixers, and other time-variant systems assume a monochromatic (single-frequency) input signal wave, where the output signal may include different frequencies as a result of the time-variant nature of the system. To accomplish such a measurement, we utilize a signal generator and a spectrum analyzer, where a monochromatic wave generated by the signal generator impinges on the metasurface through a horn antenna and the transmitted frequency-converted wave is measured by a spectrum analyzer through the second horn antenna.

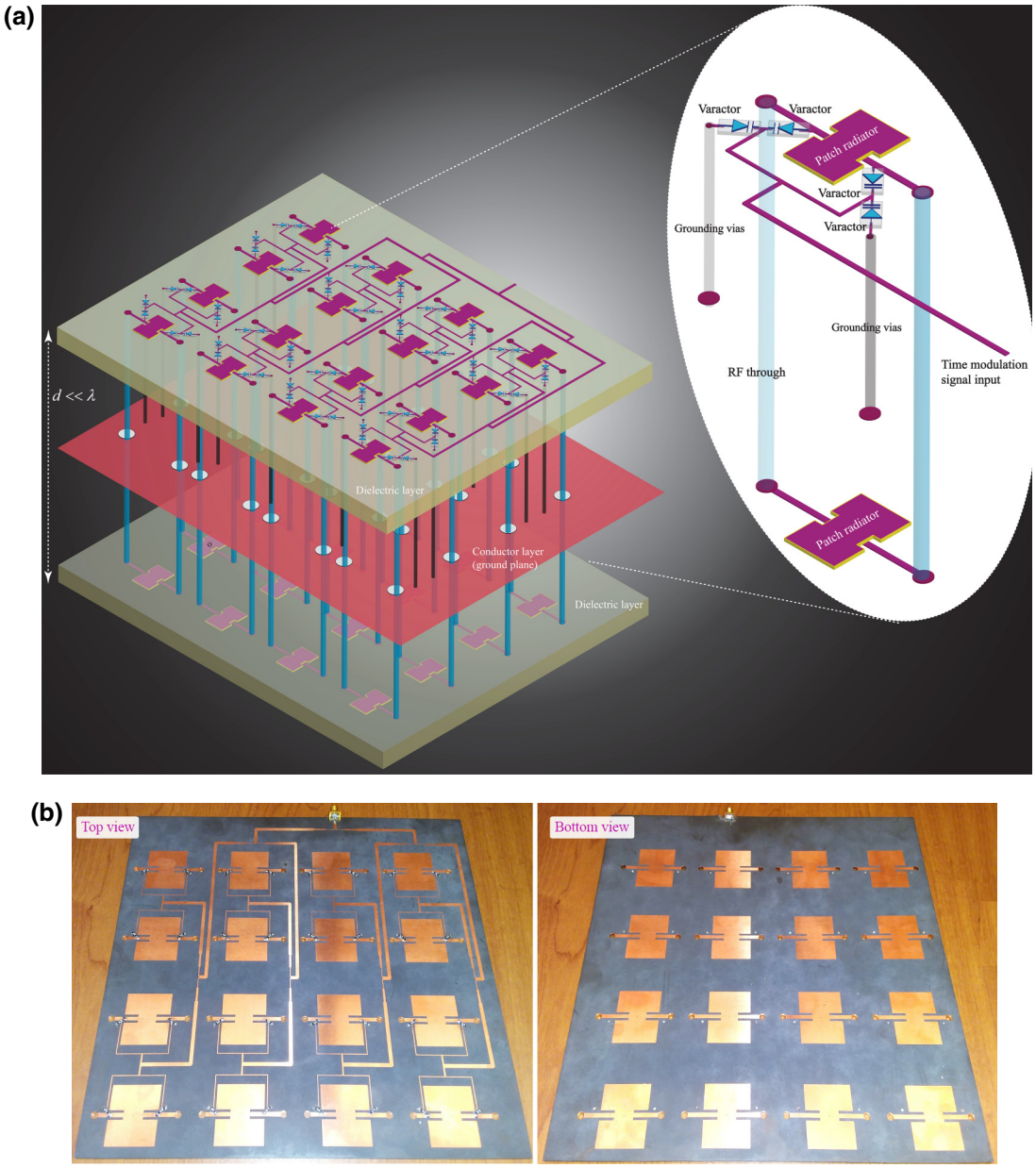

FIG. 6. Frequency-converter temporal metasurface. (a) Architecture of the complete structure. (b) Photos of the fabricated metasurface: left, top view, and right, bottom view.

Figures 9 shows the experimental setup for measuring the frequency conversion through the time-modulated metasurface. The experimental setup for the measurement of frequency conversion includes two horn antennas, two signal generators, one for the incident signal and the other for the modulation signal, a spectrum analyzer, a bias-tee for safe integration of the RF modulation bias and the DC bias of varactors, and a DC power supply.

Figures 10(a) and 10(b) plot the experimental results for the incident wave to the metasurface and transmitted frequency-up-converted wave. In this experiment, the incident signal frequency is at 2.33 GHz, the modulation frequency is at 1.06 GHz, and the transmitted up-converted signal is at 3.39 GHz. It may be seen from Fig. 10(b) that a spurious-free and linear frequency up-conversion is achieved, that is, an up-conversion from 2.33 to 3.39 GHz. The undesired mixing products are suppressed more than 36.3 dB, and the incident wave is suppressed more than 27.06 dB.

Figures 10(c) and 10(d) plot the experimental results for the incident wave to the metasurface and the transmitted frequency-down-converted wave. In this experiment, the incident signal frequency is at 5 GHz, the modulation frequency is at 1.79 GHz, and the transmitted

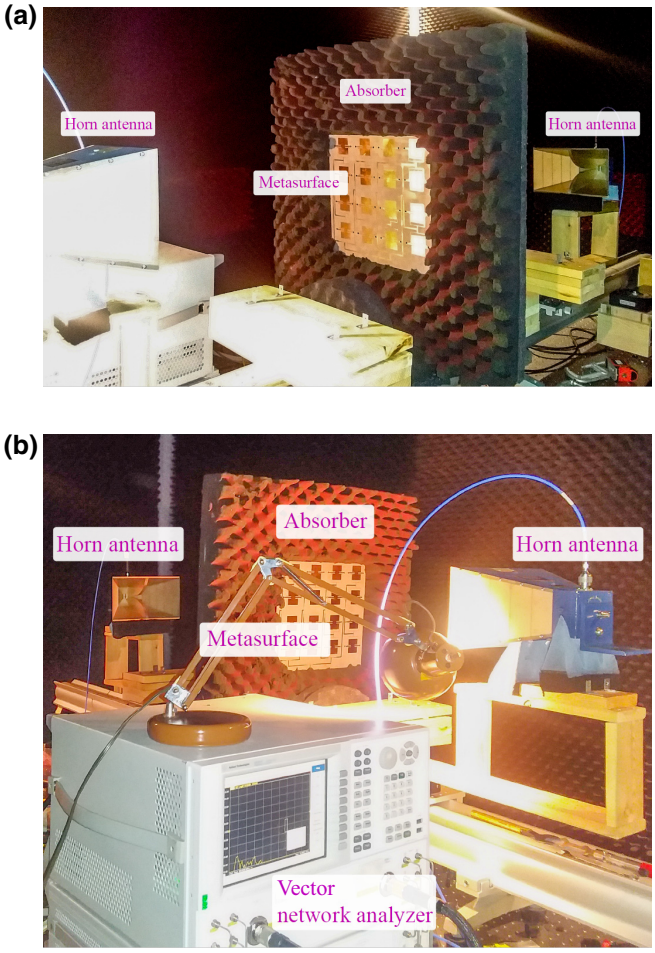

FIG. 7. Experimental setup for measuring the scattering parameters of the static metasurface, i.e., $\omega_m = 0$.

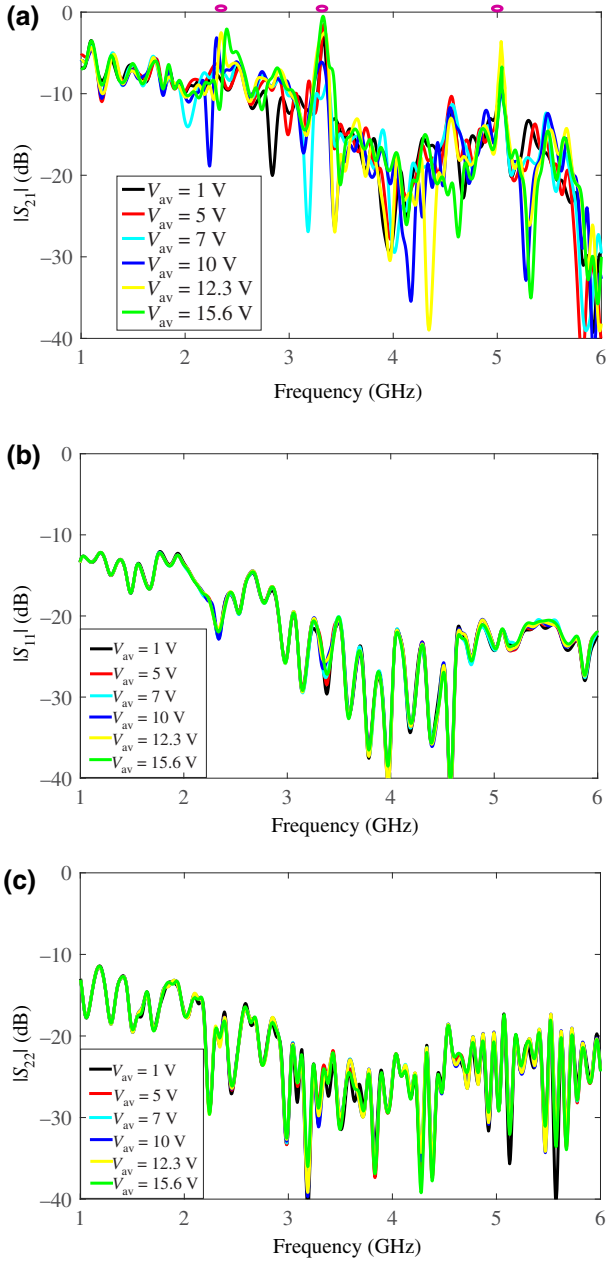

FIG. 8. Experimental scattering parameters of the nonmodulated metasurface ($\omega_m = 0$) for different voltages corresponding to different ϵ_{ant}: (a) $|S_{21}|$, (b) $|S_{11}|$, and (c) $|S_{22}|$.

up-converted signal is at 3.21 GHz. Figure 10(d) shows that a spurious-free and linear frequency down-conversion is achieved, that is, a down-conversion from 5 to 3.21 GHz. The undesired mixing products are suppressed more than 28.6 dB, and the incident wave is suppressed more than 18.1 dB. Figures 11(a) and 11(b) demonstrate linear response of the temporal metasurface for up- and down-conversions, respectively. These figures show that the frequency-converted transmitted field E_T linearly follows the incident field E_{inc}.

IV. DISCUSSION

The proposed concept and technology opens pathways towards several frequency-conversion microwave, millimeter-wave, terahertz, and nanophotonic components, without requiring cumbersome transceivers and nonlinear mixers, for a variety of applications ranging from telecommunication and biomedical systems to radio astronomy and military radars. Figure 12 shows a particular application of the frequency-converter metasurface in wireless satellite and mobile communications. In this scheme, the metasurface is mounted on top of a base station and supports wireless communication between cellular mobile phones and satellites. For instance, cellular phones may operate at Broadband Personal Communications Service (PCS band), that is, 1850–1910/1930–1990 MHz, and communicate effectively with the metasurface, whereas the metasurface converts the frequency and communicates with satellites at

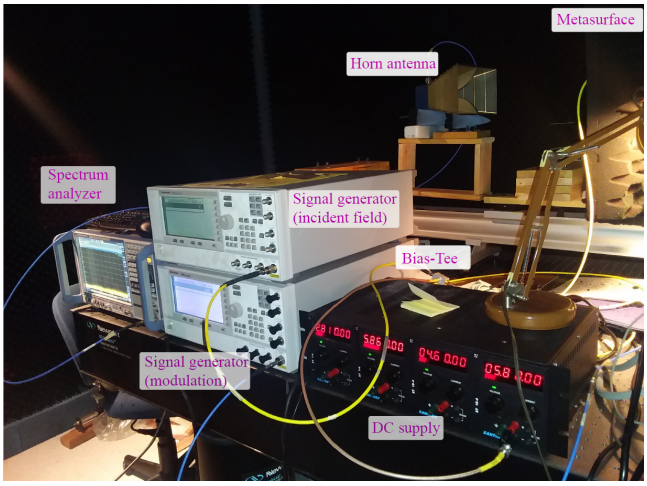

FIG. 9. Experimental setup for measuring the frequency conversion through the time-modulated metasurface.

C band, that is, 3700 and 7025 MHz, which is a well-known frequency band for satellite communications. To improve the functionality of the metasurface is this application, an appropriate beamsteering mechanism [24,64,65] may be added to the frequency-conversion functionality of the metasurface.

In contrast to conventional nonlinear mixers, the proposed frequency-converter temporal metasurface introduces a linear response, where the magnitude of the output frequency-converted signal follows the input signal magnitude. Such a linear response is endowed with time-modulation technique. The proposed frequency converter is very low profile and formed by a thin (subwavelength) metasurface slab which is paramount for practical application.

The proposed metasurface inherently provides band-pass filtering, where spurious-free and linear frequency up- and down-conversions occur in a way that the undesired time harmonics are suppressed significantly. The proposed architecture offers extra freedom in controlling the frequency bands as well as the magnitude of the converted frequency, making it an excellent apparatus for versatile wireless communication systems. We perform a proof-in-principle experiment in the microwave regime for verification. It is worth emphasizing that the proposed theory and architecture are scalable to higher frequencies.

Furthermore, such a frequency-converter metasurface can achieve conversion gain for greater pumping depths.

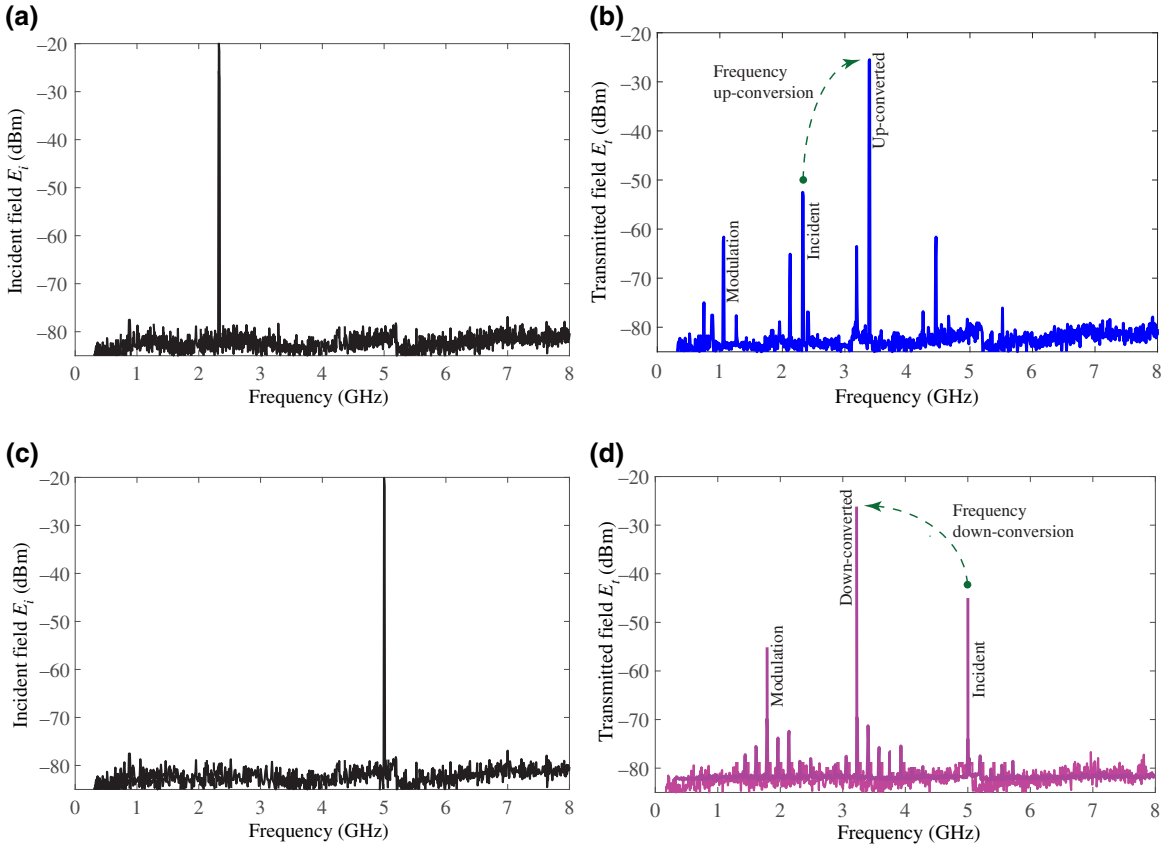

FIG. 10. Experimental results for wave transmission through the frequency-converter metasurface. (a) Incident signal at 2.33 GHz. (b) Transmitted up-converted signal at 3.39 GHz (considering a modulation frequency of 1.06 GHz). (c) Incident signal at 5 GHz. (d) Transmitted down-converted signal at 3.21 GHz (considering a modulation frequency of 1.79 GHz).

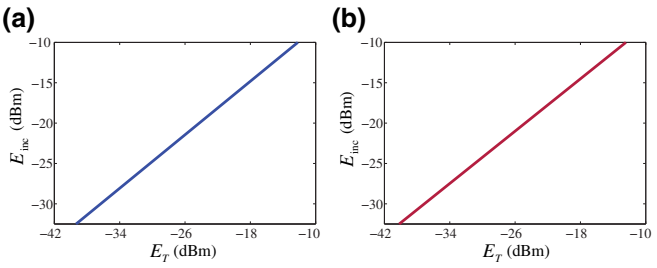

FIG. 11. Experimental results showing the linearity of the temporal frequency-converter metasurface for (a) frequency up-conversion in Fig. 10(b) and (b) frequency down-conversion in Fig. 10(d).

The magnitude of the converted signal wave at the output of the frequency converter can be further augmented by appropriate design and fabrication of the architecture. Appropriate elements may be envisioned at terahertz and optics for the realization of time modulation, e.g., using dielectric slabs doped to create *p*-*i*-*n* junction schemes responding to a modulation wave and operating as voltage-controllable capacitors [66,67].

The proposed metasurface may be extended for further signal-processing purposes, for example, for both analog and digital modulation of the converted frequencies. In the proposed proof-of-concept fabricated prototype, we apply the (LO) modulation signal wave to the front side of the metasurface [as can be seen in Fig. 6(b) (left)]. However, we do not need to apply this (LO) modulation signal wave to the back side of the metasurface [as can be seen in Fig. 6(b) (right)]. In order to add other functionalities to the metasurface, for example, analog or digital phase/amplitude modulation schemes, one may apply another analog/digital signal wave to the back side of the metasurface, where the patch elements at the back of the metasurface are loaded with Schottky, pin, or varactor diodes, depending on the application.

V. CONCLUSION

We propose a spurious-free and linear frequency-converter metasurface. Our approach to achieve metasurface-based frequency conversion utilizes transmissive temporally modulated supercells. Specifically, the presented structures are based on SIPS architectures with specifically tailored passbands and stopbands. The proposed form of modulation removes the periodicity of the time modulation, which, combined with suitably created dispersion engineering, realizes spurious-free and linear frequency conversion through a thin sheet. The proposed frequency-converter metasurface is capable of implementing large frequency-up-conversion and frequency-down-conversion ratios. Furthermore, such a spatial frequency converter is very practical, for example, in real-scenario wireless telecommunication systems, a large frequency conversion is required, that is, a frequency conversion from an intermediate frequency (VHF/UHF) to microwave frequencies in receivers. In contrast, recently proposed time-varying frequency converters suffer from very

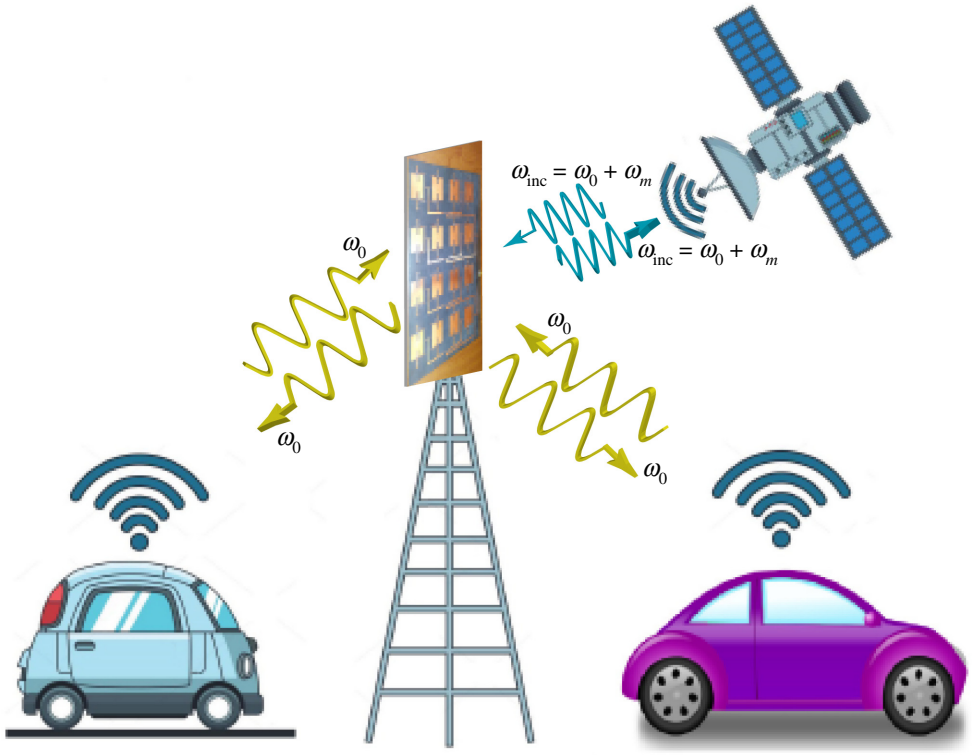

FIG. 12. Example application of a pure frequency-converter metasurface to wireless communications.

small frequency-conversion ratios (up-/down-converted frequency is very close to the input frequency) [7,19,68].

ACKNOWLEDGMENT

This work is supported by the Natural Sciences and Engineering Research Council of Canada (NSERC).

[1] Stephen A. Maas, *Microwave Mixers* (Artech House, Norwood, MA, 1993), 2nd ed.

[2] B. Henderson and E. Camargo, *Microwave Mixer Technology and Applications* (Artech House, Norwood, MA, 2013).

[3] Jun Hashimoto, Kenji Itoh, Mitsuhiro Shimozawa, and Koji Mizuno, Fundamental limitations on the output power and the third-order distortion of balanced mixers and even harmonic mixers, IEEE Trans. Microw. Theory Tech. **64**, 2853 (2016).

[4] T. Vasseaux, B. Huyart, P. Loumeau, and J. F. Naviner, in *IEEE Int. Symp. on Circ. Sys.* (Orlando, FL, USA, 1999).

[5] Holly Pekau and James W. Haslett, A 2.4 GHz CMOS subsampling mixer with integrated filtering, IEEE J. Solid-State Circ. **40**, 2159 (2005).

[6] Tianwei Jiang, Ruihuan Wu, Song Yu, Dongsheng Wang, and Wanyi Gu, Microwave photonic phase-tunable mixer, Opt. Express **25**, 4519 (2017).

[7] Sajjad Taravati and Christophe Caloz, Mixer-duplexer-antenna leaky-wave system based on periodic space-time modulation, IEEE Trans. Antennas Propag. **65**, 442 (2017).

[8] Sajjad Taravati and Ahmed A. Kishk, Dynamic modulation yields one-way beam splitting, Phys. Rev. B **99**, 075101 (2019).

[9] Xiaohu Wu, Xiaoguang Liu, Mark D. Hickle, Dimitrios Peroulis, Juan Sebastián Gómez-Díaz, and Alejandro Álvarez Melcón, Isolating bandpass filters using time-modulated resonators, IEEE Trans. Microw. Theory Tech. **67**, 2331 (2019).

[10] Sajjad Taravati and George V. Eleftheriades, Generalized Space-Time Periodic Diffraction Gratings: Theory and Applications, Phys. Rev. Appl. **12**, 024026 (2019).

[11] Yu Shi and Shanhui Fan, Dynamic non-reciprocal metasurfaces with arbitrary phase reconfigurability based on photonic transition in meta-atoms, Appl. Phys. Lett. **108**, 021110 (2016).

[12] Yu Shi, Seunghoon Han, and Shanhui Fan, Optical circulation and isolation based on indirect photonic transitions of guided resonance modes, ACS Photonics **4**, 1639 (2017).

[13] Mohammad Mahdi Salary, Samad Jafar-Zanjani, and Hossein Mosallaei, Electrically tunable harmonics in time-modulated metasurfaces for wavefront engineering, New J. Phys. **20**, 123023 (2018).

[14] Sajjad Taravati and Ahmed A. Kishk, Advanced wave engineering via obliquely illuminated space-time-modulated slab, IEEE Trans. Antennas Propag. **67**, 270 (2019).

[15] Joachim Werner Zang, Diego Correas-Serrano, J. T. S. Do, Xiaoguang Liu, Alejandro Alvarez-Melcon, and Juan Sebastian Gomez-Diaz, Nonreciprocal Wavefront Engineering with Time-Modulated Gradient Metasurfaces, Phys. Rev. Appl. **11**, 054054 (2019).

[16] Sandeep Inampudi, Mohammad Mahdi Salary, Samad Jafar-Zanjani, and Hossein Mosallaei, Rigorous space-time coupled-wave analysis for patterned surfaces with temporal permittivity modulation, Opt. Mater. Express **9**, 162 (2019).

[17] Sameh Y. Elnaggar and Gregory N. Milford, Generalized space-time periodic circuits for arbitrary structures, ArXiv:1901.08698 (2019).

[18] Neng Wang, Zhao-Qing Zhang, and C. T. Chan, Photonic Floquet media with a complex time-periodic permittivity, Phys. Rev. B **98**, 085142 (2018).

[19] Zhanni Wu and Anthony Grbic, Serrodyne frequency translation using time-modulated metasurfaces, IEEE Trans. Antennas Propag. **68**, 1599 (2019).0018-926X

[20] Sajjad Taravati and Ahmed A. Kishk, Space-time modulation: Principles and applications, IEEE Microw. Mag. **21**, 30 (2020).

[21] Grigorii A. Ptitcyn, Mohammad Sajjad Mirmoosa, and Sergei A. Tretyakov, Time-modulated meta-atoms, Phys. Rev. Res. **1**, 023014 (2019).

[22] Zhi-Xia Du, Aobo Li, Xiu Yin Zhang, and Daniel F. Sievenpiper, A simulation technique for radiation properties of time-varying media based on frequency-domain solvers, IEEE Access **7**, 112375 (2019).

[23] Xuchen Wang, Ana Diaz-Rubio, Huanan Li, Sergei A. Tretyakov, and Andrea Alu, Theory and Design of Multifunctional Space-Time Metasurfaces, Phys. Rev. Appl. **13**, 044040 (2020).

[24] Sajjad Taravati and George V. Eleftheriades, Full-Duplex Nonreciprocal Beam Steering by Time-Modulated Phase-Gradient Metasurfaces, Phys. Rev. Appl. **14**, 014027 (2020).

[25] Sameh Y. Elnaggar and Gregory N. Milford, Modeling space–time periodic structures with arbitrary unit cells using time periodic circuit theory, IEEE Trans. Antennas Propag. **68**, 6636 (2020).

[26] Aobo Li, Yunbo Li, Jiang Long, Ebrahim Forati, Zhixia Du, and Dan Sievenpiper, Time-moduated nonreciprocal metasurface absorber for surface waves, Opt. Lett. **45**, 1212 (2020).

[27] Davide Ramaccia, Dimitrios L. Sounas, Angelica V. Marini, Alessandro Toscano, and Filiberto Bilotti, Electromagnetic isolation induced by time-varying metasurfaces: Nonreciprocal Bragg grating, IEEE Antennas Wirel. Propag. Lett. **19**, 1886 (2020).

[28] Sajjad Taravati and George V. Eleftheriades, Four-dimensional wave transformations by space-time metasurfaces, ArXiv:2011.08423 (2020).

[29] Prasad Jayathurathnage, Fu Liu, Mohammad S. Mirmoosa, Xuchen Wang, Romain Fleury, and Sergei A. Tretyakov, Time-varying components for enhancing wireless transfer of power and information, ArXiv:2011.00262 (2020).

[30] Hooman Barati Sedeh, Mohammad Mahdi Salary, and Hossein Mosallaei, Adaptive multichannel terahertz communication by space-time shared aperture metasurfaces, IEEE Access **8**, 185919 (2020).

[31] Zhanni Wu, Cody Scarborough, and Anthony Grbic, Space-Time-Modulated Metasurfaces with Spatial Discretization: Free-Space *n*-Path Systems, Phys. Rev. Appl. **14**, 064060 (2020).

[32] D. Ramaccia, A. Alù, A. Toscano, and F. Bilotti, Temporal multilayer structures for designing higher-order transfer

functions using time-varying metamaterials, Appl. Phys. Lett. **118**, 101901 (2021).
[33] John L. Wentz, A nonreciprocal electrooptic device, Proc. IEEE **54**, 97 (1966).
[34] Sajjad Taravati, Nima Chamanara, and Christophe Caloz, Nonreciprocal electromagnetic scattering from a periodically space-time modulated slab and application to a quasisonic isolator, Phys. Rev. B **96**, 165144 (2017).
[35] Sajjad Taravati, Self-biased broadband magnet-free linear isolator based on one-way space-time coherency, Phys. Rev. B **96**, 235150 (2017).
[36] Sajjad Taravati, Giant Linear Nonreciprocity, Zero Reflection, and Zero Band Gap in Equilibrated Space-Time-Varying Media, Phys. Rev. Appl. **9**, 064012 (2018).
[37] Mourad Oudich, Yuanchen Deng, Molei Tao, and Yun Jing, Space-time phononic crystals with anomalous topological edge states, Phys. Rev. Res. **1**, 033069 (2019).
[38] Mahdi Chegnizadeh, Mohammad Memarian, and Khashayar Mehrany, Non-reciprocity using quadrature-phase time-varying slab resonators, J. Opt. Soc. Am. B **37**, 88 (2020).
[39] Saiiad Taravati and George V. Eleftheriades, in *2020 Fourteenth International Congress on Artificial Materials for Novel Wave Phenomena (Metamaterials)* (IEEE, New York), p. 081.
[40] Xuchen Wang, Grigorii Ptitcyn, V. S. Asadchy, A. Díaz-Rubio, Mohammad Sajjad Mirmoosa, Shanhui Fan, and Sergei A. Tretyakov, Nonreciprocity in Bianisotropic Systems with Uniform Time Modulation, Phys. Rev. Lett. **125**, 266102 (2020).
[41] Sajjad Taravati and George V. Eleftheriades, in *2020 Fourteenth International Congress on Artificial Materials for Novel Wave Phenomena (Metamaterials)* (IEEE, New York), p. 066.
[42] Sajjad Taravati, Aperiodic space-time modulation for pure frequency mixing, Phys. Rev. B **97**, 115131 (2018).
[43] Hershel Shanks, A new technique for electronic scanning, IEEE Trans. Antennas Propag. **9**, 162 (1961).
[44] Jiawei Zang, Xuetian Wang, Alejandro Alvarez-Melcon, and Juan Sebastian Gomez-Diaz, Nonreciprocal Yagi–Uda filtering antennas, IEEE Antennas Wirel. Propag. Lett. **18**, 2661 (2019).
[45] Peter Halevi, Jorge R. Zurita-Sánchez, and Juan C. Cervantes-González, Reflection and transmission of a wave incident on a slab with a time-periodic dielectric function $\epsilon(t)$, Phys. Rev. A **79**, 053821 (2009).
[46] Junfei Li, Chen Shen, Xiaohui Zhu, Yangbo Xie, and Steven A. Cummer, Nonreciprocal sound propagation in space-time modulated media, Phys. Rev. B **99**, 144311 (2019).
[47] Diego Correas Serrano, Andrea Alù, and Juan Sebastian Gomez-Diaz, Magnetic-free nonreciprocal photonic platform based on time-modulated graphene capacitors, Phys. Rev. B **98**, 165428 (2018).
[48] Lei Zhang, Xiao Qing Chen, Shuo Liu, Qian Zhang, Jie Zhao, Jun Yan Dai, Guo Dong Bai, Xiang Wan, Qiang Cheng, Giuseppe Castaldi, *et al.*, Space-time-coding digital metasurfaces, Nat. Commun. **9**, 4334 (2018).
[49] Mingkai Liu, David A. Powell, Yair Zarate, and Ilya V. Shadrivov, Huygens' Metadevices for Parametric Waves, Phys. Rev. X **8**, 031077 (2018).
[50] Sameh Y. Elnaggar and Gregory N. Milford, Modelling space-time periodic structures with arbitrary unit cells using time periodic circuit theory, ArXiv:1901.08698 (2019).
[51] Sajjad Taravati and George V. Eleftheriades, Space-Time Medium Functions as a Perfect Antenna-Mixer-Amplifier Transceiver, Phys. Rev. Appl. **14**, 054017 (2020).
[52] Xiaohui Zhu, Junfei Li, Chen Shen, Guangyu Zhang, Steven A. Cummer, and Longqiu Li, Tunable unidirectional compact acoustic amplifier via space-time modulated membranes, Phys. Rev. B **102**, 024309 (2020).
[53] Peixin Chu, Junxue Chen, Zhonggang Xiong, and Zao Yi, Controllable frequency conversion in the coupled time-modulated cavities with phase delay, Opt. Commun. **476**, 126338 (2020).
[54] José Gabriel Gaxiola-Luna and P. Halevi, Temporal photonic (time) crystal with a square profile of both permittivity ϵ(t) and permeability μ(t), Phys. Rev. B **103**, 144306 (2021).
[55] Ville Tiukuvaara, Tom J. Smy, and Shulabh Gupta, Floquet analysis of space-time modulated metasurfaces with Lorentz dispersion, IEEE Trans. Antennas Propag. (2021).
[56] Diego M. Solís and Nader Engheta, Functional analysis of the polarization response in linear time-varying media: A generalization of the Kramers-Kronig relations, Phys. Rev. B **103**, 144303 (2021).
[57] Edwards S. Cassedy and Arthur A. Oliner, Dispersion relations in time-space periodic media: Part I—Stable interactions, Proc. IEEE **51**, 1342 (1963).
[58] Ramesh Garg, Prakash Bhartia, Inder Bahl, and Apisak Ittipiboon, *Microstrip Antenna Design Handbook* (Artech House, Norwood, MA, 2001).
[59] Weng Cho Chew, *Waves and Fields in Inhomogeneous Media* (IEEE Press, Piscataway, New Jersey, 1995), Vol. 522.
[60] Edward F. Kuester, Mohamed A. Mohamed, Melinda Piket-May, and Christopher L. Holloway, Averaged transition conditions for electromagnetic fields at a metafilm, IEEE Trans. Antennas Propag. **51**, 2641 (2003).
[61] M. Mithat Idemen, *Discontinuities in the Electromagnetic Field* (John Wiley & Sons, Hoboken, New Jersey, 2011), Vol. 40.
[62] K. Achouri, Mohamed Ahmed Salem, and C. Caloz, General metasurface synthesis based on susceptibility tensors, IEEE Trans. Antennas Propag. **63**, 2977 (2015).
[63] Yakir Hadad, Dimitrios L. Sounas, and Andrea Alù, Space-time gradient metasurfaces, Phys. Rev. B **92**, 100304 (2015).
[64] Sajjad Taravati and George V. Eleftheriades, Full-duplex reflective beamsteering metasurface featuring magnetless nonreciprocal amplification, ArXiv:2101.10067 (2021).
[65] Sajjad Taravati and George V. Eleftheriades, Programmable nonreciprocal meta-prism, Sci. Rep. **11**, 1 (2021).
[66] Anatol Khilo, Cheryl M. Sorace, and Franz X. Kärtner, Broadband linearized silicon modulator, Opt. Express **19**, 4485 (2011).
[67] Hugo Lira, Zongfu Yu, and Shanhui Fan, and Michal Lipson, Electrically Driven Nonreciprocity Induced by Interband Photonic Transition on a Silicon Chip, Phys. Rev. Lett. **109**, 033901 (2012).
[68] Sajjad Taravati and Christophe Caloz, in *IEEE AP-S Int. Antennas Propagat. (APS)* (Vancouver, Canada, 2015).